

Article

Binary Nitrogen Precursor-Derived Porous Fe-N-S/C Catalyst for Efficient Oxygen Reduction Reaction in a Zn-Air Battery

Xiao Liu ^{1,2}, **Chi Chen** ¹, **Qingqing Cheng** ^{1,2}, **Liangliang Zou** ¹, **Zhiqing Zou** ^{1,*} and **Hui Yang** ^{1,*}¹ Shanghai Advanced Research Institute, Chinese Academy of Sciences, Shanghai 201210, China; liuxiao@sari.ac.cn (X.L.); chenchi@sari.ac.cn (C.C.); chengqinghc@163.com (Q.C.); zoull@sari.ac.cn (L.Z.)² University of the Chinese Academy of Sciences, Beijing 100039, China

* Correspondence: zouzq@sari.ac.cn (Z.Z.); yangh@sari.ac.cn (H.Y.); Tel.: +86-21-2032-4112 (H.Y.)

Received: 2 March 2018; Accepted: 19 March 2018; Published: 13 April 2018



Abstract: It is still a challenge to synthesize non-precious-metal catalysts with high activity and stability for the oxygen reduction reaction (ORR) to replace the state-of-the art Pt/C catalyst. Herein, a Fe, N, S co-doped porous carbon (Fe-NS/PC) is developed by using g-C₃N₄ and 2,4,6-tri(2-pyridyl)-1,3,5-triazine (TPTZ) as binary nitrogen precursors. The interaction of binary nitrogen precursors not only leads to the formation of more micropores, but also increases the doping amount of both iron and nitrogen dispersed in the carbon matrix. After a second heat-treatment, the best Fe/NS/C-g-C₃N₄/TPTZ-1000 catalyst exhibits excellent ORR performance with an onset potential of 1.0 V vs. reversible hydrogen electrode (RHE) and a half-wave potential of 0.868 V (RHE) in alkaline medium. The long-term durability is even superior to the commercial Pt/C catalyst. In the meantime, an assembled Zn-air battery with Fe/NS/C-g-C₃N₄/TPTZ-1000 as the cathode shows a maximal power density of 225 mW·cm⁻² and excellent durability, demonstrating the great potential of practical applications in energy conversion devices.

Keywords: non-precious metal catalyst; oxygen reduction reaction; binary nitrogen precursors; g-C₃N₄; 2,4,6-tri(2-pyridyl)-1,3,5-triazine

1. Introduction

The oxygen reduction reaction (ORR) plays an important role in the energy efficiency of polymer electrolyte membrane fuel cells (PEMFCs) and metal-air batteries (MABs). So far, platinum (Pt)-based materials are still the most effective catalysts for the ORR due to its sluggish kinetics. However, the high price and scarcity of Pt severely hinder the large-scale applications of PEMFCs and MABs. Therefore, extensive efforts have been devoted to develop low-cost and earth-abundant non-precious metal catalysts with efficient ORR performance. The transition metal (M=Fe, Co, etc.) and nitrogen co-doped carbon materials (M-N-C), such as graphene [1,2], nanotube [3,4], and porous carbon [5,6], have shown great progress in ORR electrocatalysis, especially for Fe-N-C materials, which have been considered as the most promising catalysts for substituting the expensive Pt catalysts [7–9].

The excellent ORR activity usually depends on two main factors, namely, the high intrinsic activity of single sites and high density of active sites. Therefore, the M-N-C electrocatalysts for efficient ORR require high heteroatom doping contents, high surface area, porous structure, and good conductivity [10–12]. Heteroatom doping is an effective method to tailor the electronic structure of electroneutral carbon matrix, which would facilitate the adsorption of O₂. High surface area and porous structure are beneficial to increase the number of accessible active sites and facilitate the mass transport of the ORR relevant species approaching the internal active sites of catalysts [13,14]. Heat-treatment

at high temperature is a vital process to form the ORR active centers, therefore, the precursors should be chosen carefully. Recently, the use of binary nitrogen precursors has been developed as an effective synthetic strategy to improve the porosity and heteroatoms doping contents, hence to improve the ORR activity. Wu et al. [15] synthesized a Fe-N-C catalyst derived from polyaniline (PANI) and dicyandiamide (DCDA) as binary nitrogen precursors, which possessed higher ORR activity than the individual PANI or DCDA-derived ones. The superior ORR activity can be ascribed to the increased content of pyridinic nitrogen doped into the carbon matrix. The combination of PANI and DCDA could enhance the porosity and increase the surface area, thanks to the different decomposition temperatures. Chen et al. [16] synthesized a class of Fe-N-C catalysts with 3D nanoporous structure using phenanthroline (Phen) and PANI as dual nitrogen sources. The Phen played the role of pore-creating agent due to its lower thermostability. A similar strategy was also reported by Zelenay et al. [17]. Moreover, it has been proved that the additional doping of S atoms in the Fe-N-C catalyst will remarkably enhance the ORR activity [18]. However, although the development of non-precious metal catalysts has achieved great progress, the application of these materials in practical devices, such as PEMFCs and MABs, is still far from satisfactory, especially for the long-term stability [19].

In this work, we have developed a facile method to synthesize Fe, N, S co-doped porous carbon materials (Fe-NS/PC) as efficient ORR catalysts with g-C₃N₄ and 2,4,6-tri(2-pyridyl)-1,3,5-triazine (TPTZ) as binary nitrogen precursors. The TPTZ is able to coordinate with Fe³⁺ [20], which could contribute to the uniformly-dispersed metal-containing species located at the N-doped carbon skeleton [21,22]. The addition of g-C₃N₄ sheets could inhibit the sintering of TPTZ during carbonization. The interaction of g-C₃N₄ and TPTZ is beneficial to increase the doping amount of iron and nitrogen, and to facilitate the mass transfer of ORR relevant species. As a result, the binary nitrogen precursor-derived Fe-NS/PC catalyst exhibited better ORR performance than the single nitrogen precursor-derived ones. After second heat treatment, the Fe/NS/C-g-C₃N₄/TPTZ catalyst shows enhanced activity and long-term durability. The best ORR activity of Fe/NS/C-g-C₃N₄/TPTZ-1000 is even superior to that of the state-of-the art Pt/C catalyst. A Zn-air battery with the Fe/NS/C-g-C₃N₄/TPTZ-1000 cathode exhibits a maximal power density of 225 mW·cm⁻² at room temperature and superior stability with only 4.03% loss of output voltage at a current density of 20 mA·cm⁻² after 20,000 s.

2. Results and Discussion

Figure 1a–c show the scanning electron microscope (SEM) images of the as-synthesized Fe-NS/PC catalysts using g-C₃N₄ and TPTZ separated as single nitrogen precursor and together as binary nitrogen precursors, denoted as Fe/NS/C-g-C₃N₄, Fe/NS/C-TPTZ, and Fe/NS/C-g-C₃N₄/TPTZ, respectively. The Fe/NS/C-g-C₃N₄ has a fluffy morphology with high porosity (Figure 1a). By contrast, Fe/NS/C-TPTZ shows a denser morphology (Figure 1b), probably because of the collapse of the carbon skeleton during heat-treatment. Through the combination of both g-C₃N₄ and TPTZ with various thermal stability (Figure S1), the Fe/NS/C-g-C₃N₄/TPTZ preserves the fluffy morphology (Figure 1c), probably due to the fact that the mixed g-C₃N₄ sheets prevent the sintering of TPTZ.

The effects of N precursors on BET surface areas and pore structures were studied by N₂ adsorption-desorption isotherms. As can be seen in Figure 1d,f, the Fe/NS/C-g-C₃N₄ exhibits a highest BET surface area of 928 m²/g, the most of which are external surface area. The micropore area is only 82 m²/g. The Fe/NS/C-TPTZ shows a slightly lower BET surface area of 849 m²/g, but a much larger micropore area of 317 m²/g. However, the amounts of mesopores and macropores are relatively few (Figure 1e), which are consistent with the dense structure displayed by SEM image (Figure 1b). After the combination of g-C₃N₄ and TPTZ, although the BET surface area slightly decreases (759 m²/g), the Fe/NS/C-g-C₃N₄/TPTZ catalyst integrates the micropores of Fe/NS/C-TPTZ and the fluffy structure of Fe/NS/C-g-C₃N₄ (Figure 1f), which might facilitate the mass transfer and the ORR catalytic activity [23,24].

X-ray diffraction (XRD) was carried out to characterize the crystal structure of the Fe-NS/PC catalysts. According to the XRD patterns in Figure 1g, the Fe/NS/C-TPTZ exhibits two main diffraction peaks at around 25.5° and 43° , associated to the (002) and (100) planes of graphitic carbon, respectively. The (002) diffraction peak of the Fe/NS/C-g-C₃N₄ shifts to a higher angle of 29.8° , which can be associated with the carbon nitride (PDF-#78-1747). Noteworthy, the binary nitrogen precursor-derived Fe/NS/C-g-C₃N₄/TPTZ displays a broad peak at around 25.8° corresponding to the (002) diffraction of graphitic carbon, and a weak swell at 29.8° corresponding to the carbon nitride, which clearly indicates the interaction between two nitrogen precursors during pyrolysis. No other diffraction peaks can be observed, demonstrating the absence of any other Fe-containing crystalline phases.

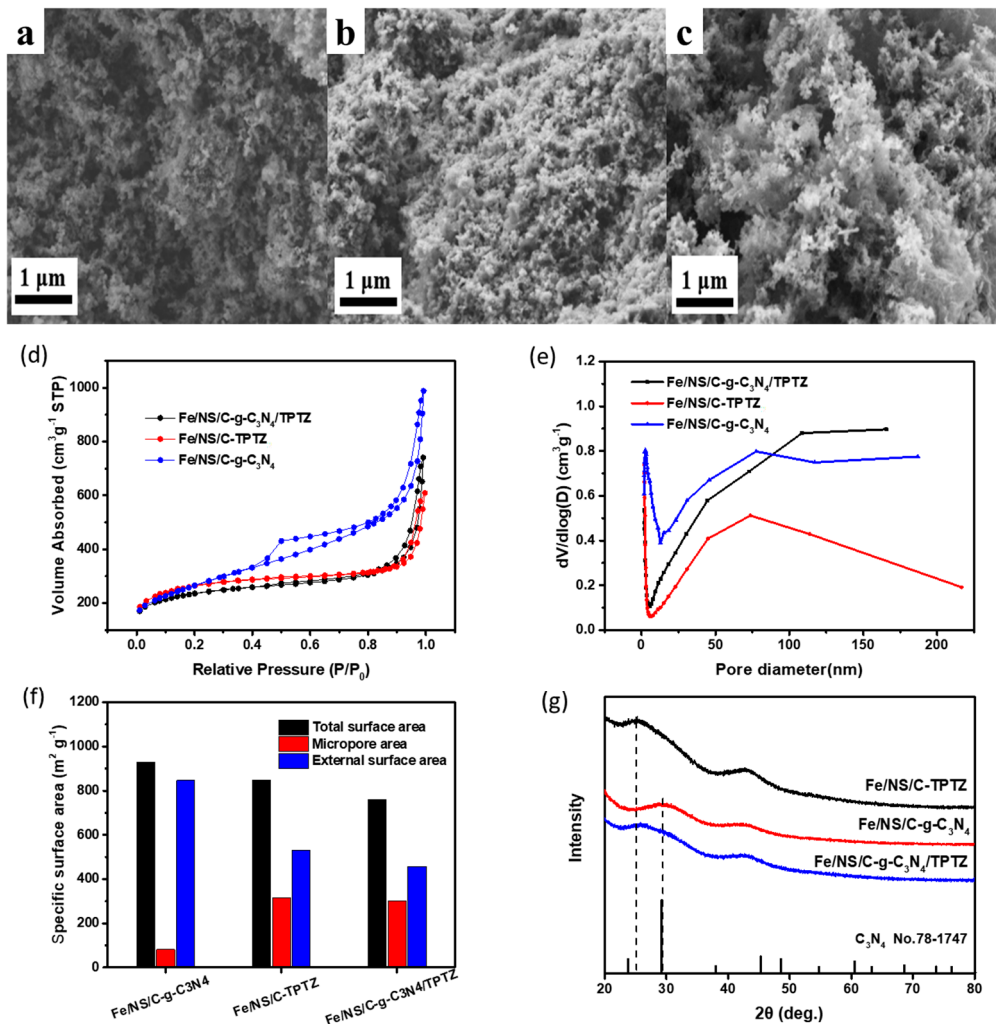


Figure 1. Scanning electron microscope (SEM) images of (a) Fe/NS/C-g-C₃N₄, (b) Fe/NS/C-TPTZ (TPTZ: 2,4,6-tri(2-pyridyl)-1,3,5-triazine), and (c) Fe/NS/C-g-C₃N₄/TPTZ; (d) N₂ adsorption-desorption isotherms; (e) corresponding pore size distributions; (f) comparison of BET surface areas; and (g) X-ray diffraction (XRD) patterns of Fe/NS/C-g-C₃N₄, Fe/NS/C-TPTZ, and Fe/NS/C-g-C₃N₄/TPTZ.

X-ray photoelectron spectroscopy (XPS) was implemented to investigate the states of each component within the Fe-NS/PC catalysts. The survey XPS spectra (Figure 2a) reveal that the main elements of Fe-NS/PC catalysts consist of Fe, N, C, O, and S. The elemental compositions are summarized in Table S1. Figure 2b–d display the high resolution N 1s spectra of the three Fe-NS/PC catalysts. All the spectra can be deconvoluted into four peaks corresponding to pyridinic N (N1,

398.1–398.7 eV), pyrrolic N (N2, 399.78–400.7 eV), graphitic N (N3, 400.99–401.3 eV), and oxidized N (N4, 402–404.27 eV) [25,26], respectively. Previous reports have demonstrated that both pyridinic N and graphitic N may participate the oxygen reduction reaction [27–29]. These two N species (N1 + N3) account for 4.03 at% of all the elements in Fe/NS/C-g-C₃N₄/TPTZ, remarkably higher than that of Fe/NS/C-g-C₃N₄ (1.88%) and Fe/NS/C-TPTZ (3.46%), as shown in Table S1. Notably, the contents of Fe and N in Fe/NS/C-g-C₃N₄/TPTZ are 0.29 at% and 6.67 at%, respectively, both of which are the highest among the three catalysts. In addition, the co-doping of S element in Fe-N-C catalysts would further improve the ORR activity, probably due to the structural defects and electron distribution induced by S atoms [30,31]. Based on the consideration of the high heteroatoms doping contents combined with the porous structure, the high ORR activity could be expected for the Fe/NS/C-g-C₃N₄/TPTZ catalyst.

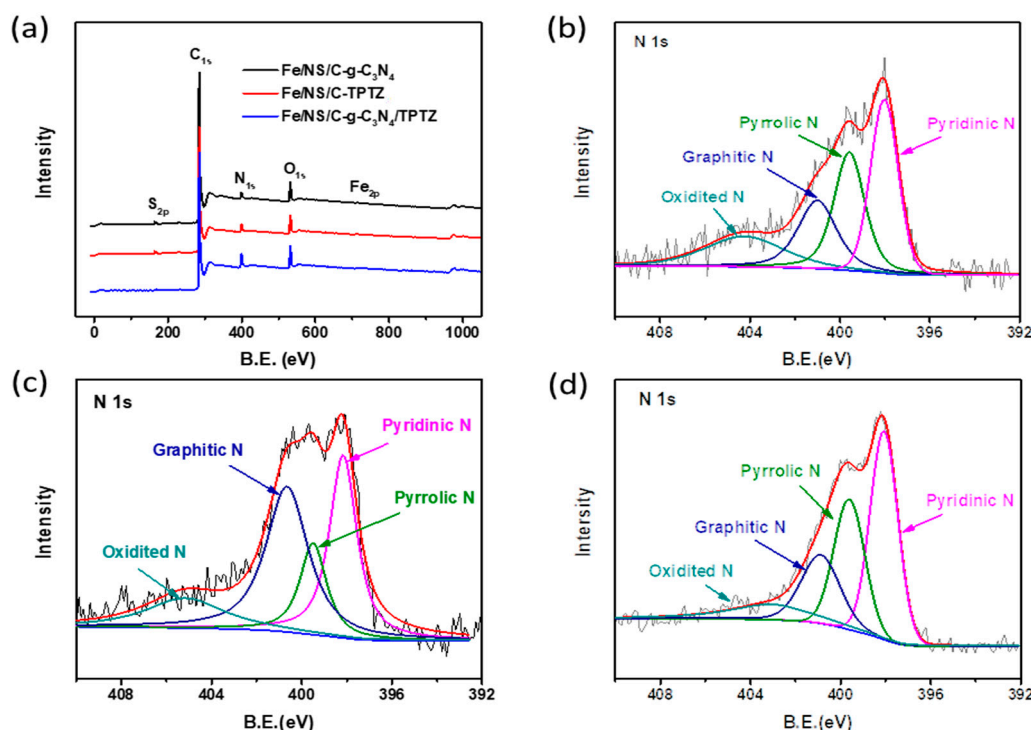


Figure 2. (a) X-ray photoelectron spectroscopy (XPS) survey spectra of Fe/NS/C-g-C₃N₄, Fe/NS/C-TPTZ, and Fe/NS/C-g-C₃N₄/TPTZ catalysts; high-resolution N 1s XPS spectra of (b) Fe/NS/C-g-C₃N₄, (c) Fe/NS/C-TPTZ, and (d) Fe/NS/C-g-C₃N₄/TPTZ.

The ORR activity of the Fe-NS/PC catalysts were evaluated by rotating disk electrode (RDE) test in O₂-saturated 0.1 M KOH solution. As displayed in Figure 3, the Fe/NS/C-g-C₃N₄/TPTZ catalyst exhibits the best ORR activity with an onset (E_0) and half-wave ($E_{1/2}$) potential of 0.95 V and 0.853 V (RHE), respectively, higher than that of Fe/NS/C-g-C₃N₄ catalyst ($E_0 = 0.946$ V and $E_{1/2} = 0.843$ V). By sharp contrast, the Fe/NS/C-TPTZ shows inferior ORR activity with $E_0 = 0.917$ V (RHE) and much smaller diffusion-limited current, probably due to the agglomerations of sintered carbon that are difficult to disperse obstruct the transfer of ORR-related species, in spite of the high BET surface area. The presence of g-C₃N₄ in dual nitrogen precursors might avoid the sintering of TPTZ, meanwhile maintain the fluffy structure and increase the Fe, N doping content, thus resulting in the full exposure of active sites, which could be responsible for the high ORR activity of the Fe/NS/C-g-C₃N₄/TPTZ catalyst.

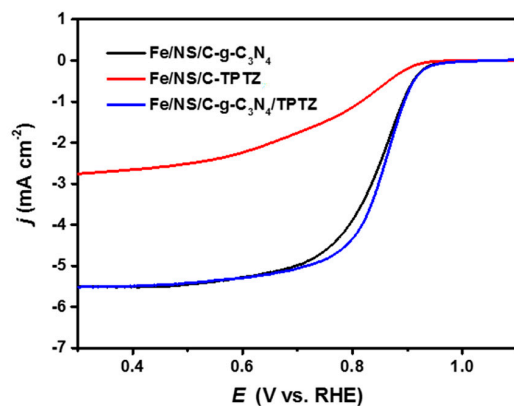


Figure 3. Oxygen reduction reaction (ORR) polarization curves of Fe/NS/C-g-C₃N₄, Fe/NS/C-TPTZ, and Fe/NS/C-g-C₃N₄/TPTZ catalysts in O₂-saturated 0.1 M KOH with a rotating speed of 1600 rpm and at a scan rate of 10 mV s⁻¹. RHE: reversible hydrogen electrode.

To further improve the ORR performance, a secondary heat treatment was conducted to the best Fe/NS/C-g-C₃N₄/TPTZ catalyst at the range of 800–1000 °C, denoted as Fe/NS/C-g-C₃N₄/TPTZ-T (T = 800, 900, 1000). Figure 4a–h present the transmission electron microscope (TEM) images of Fe/NS/C-g-C₃N₄/TPTZ, and Fe/NS/C-g-C₃N₄/TPTZ-T (T = 800, 900, 1000) at diverse magnifications. All these samples show the morphological characteristics of agglomerations of amorphous carbon nanoparticles with the diameter of 20–50 nm. No crystalline iron-containing nanoparticles can be observed for all three catalysts, indicating no agglomerations of iron formed during the second heat treatment. The energy dispersive X-ray spectroscopy (EDX) mapping analysis of Fe/NS/C-g-C₃N₄/TPTZ-1000 was also carried out to observe the elemental distributions. As can be seen in Figure 4i, the TEM image and the corresponding elemental mapping reveal that all doping heteroatoms, which are regarded as the components of the ORR active sites, are uniformly distributed throughout the carbon matrix, leading to the full exposure of the active sites to the ORR related species.

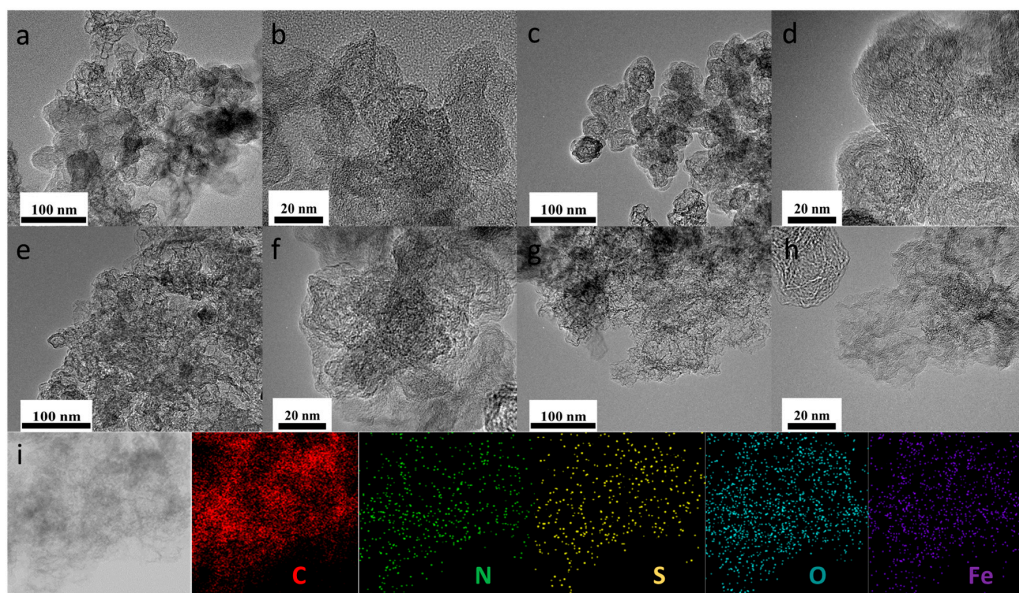


Figure 4. Transmission electron microscope (TEM) images of (a,b) Fe/NS/C-g-C₃N₄/TPTZ; (c,d) Fe/NS/C-g-C₃N₄/TPTZ-800; (e,f) Fe/NS/C-g-C₃N₄/TPTZ-900; (g,h) Fe/NS/C-g-C₃N₄/TPTZ-1000; and (i) TEM-EDX (EDX: energy dispersive X-ray spectroscopy) mapping analysis of C, N, S, O, and Fe of Fe/NS/C-g-C₃N₄/TPTZ-1000.

After a second heat treatment at different temperatures, all three Fe/NS/C-g-C₃N₄/TPTZ-T (T = 800, 900, 1000) catalysts show two main diffraction peaks at around 29.8° and 43° (Figure 5a), similar to Fe/NS/C-g-C₃N₄. There are no other diffraction peaks appear, further demonstrating the absence of crystalline iron-containing phases, which is consistent with the TEM results (Figure 4). Figure 5b displays the N₂ adsorption-desorption isotherms of the Fe/NS/C-g-C₃N₄/TPTZ-T (T = 800, 900, 1000) catalysts. The BET surface areas of Fe/NS/C-g-C₃N₄/TPTZ-800, Fe/NS/C-g-C₃N₄/TPTZ-900, and Fe/NS/C-g-C₃N₄/TPTZ-1000 are 876.8 m² g⁻¹, 1026.4 m² g⁻¹, 1138.9 m² g⁻¹, respectively. The pore size distributions of the Fe/NS/C-g-C₃N₄/TPTZ-T (T = 800, 900, 1000) indicate that the three catalysts all possess a good porous structure (Figure 5c).

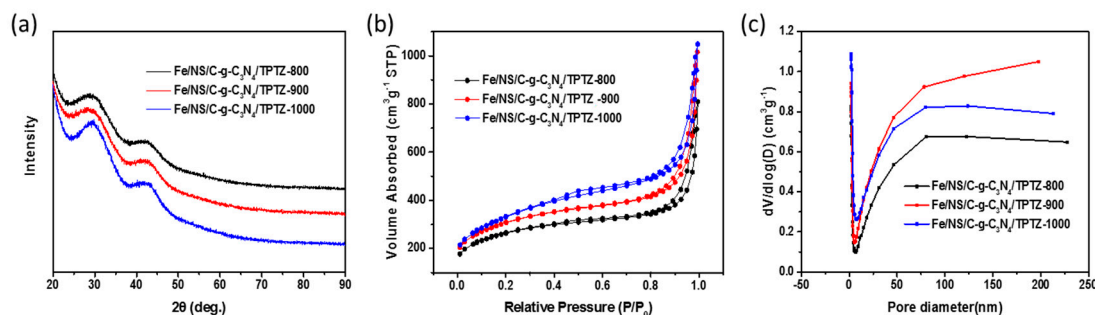


Figure 5. (a) XRD patterns; (b) N₂ adsorption-desorption isotherms; and (c) corresponding pore size distributions of Fe/NS/C-g-C₃N₄/TPTZ-800, Fe/NS/C-g-C₃N₄/TPTZ-900, and Fe/NS/C-g-C₃N₄/TPTZ-1000.

The XPS survey spectra of Fe/NS/C-g-C₃N₄/TPTZ and Fe/NS/C-g-C₃N₄/TPTZ-T (T = 800, 900, 1000) were collected to measure the elemental compositions, as shown in Figure 6a and Table S2. The contents of doped Fe and N elements reduce along with the secondary heat treatment temperature elevates. The N doping contents of Fe/NS/C-g-C₃N₄/TPTZ-T (T = 800, 900, 1000) are 4.48%, 2.57%, and 1.40%, respectively, all lower than that of Fe/NS/C-g-C₃N₄/TPTZ, due to the formation of gaseous N-containing phases. The deconvoluted high-resolution N 1s spectra reveal that the pyridinic N and graphitic N predominate in all three catalysts, as shown in Figure 6b–d and summarized in Table S2. The high-resolution S 2p spectrum of Fe/NS/C-g-C₃N₄/TPTZ-1000 can be deconvoluted into three peaks, as shown in Figure 6e. The two peaks at 164.0 and 165.2 eV can be described to S 2p_{3/2} and S 2p_{1/2} of thiophene-like C-S-C structure, respectively [32,33], while the third peak at 167.3 eV corresponds to sulfate species. The synergetic effects of N, S co-doping would significantly improve the ORR activity by reducing the electron localization around the Fe centers, and improve the interaction with oxygen, facilitating the four-electron pathway [34]. The high-resolution Fe 2p spectrum of Fe/NS/C-g-C₃N₄/TPTZ-1000 presents two major peaks at around 711 and 724 eV, corresponding to Fe 2p_{1/2} and Fe 2p_{3/2}, respectively (Figure 6f) [15,35]. The dominant peak at 711 eV can be assigned to Fe³⁺ or Fe²⁺ coordinated with N, which are suggested to be the ORR active centers [15,36]. The peak at 718.5 eV is a satellite peak indicating the co-existence of Fe³⁺ and Fe²⁺ in the Fe/NS/C-g-C₃N₄/TPTZ-1000 [35].

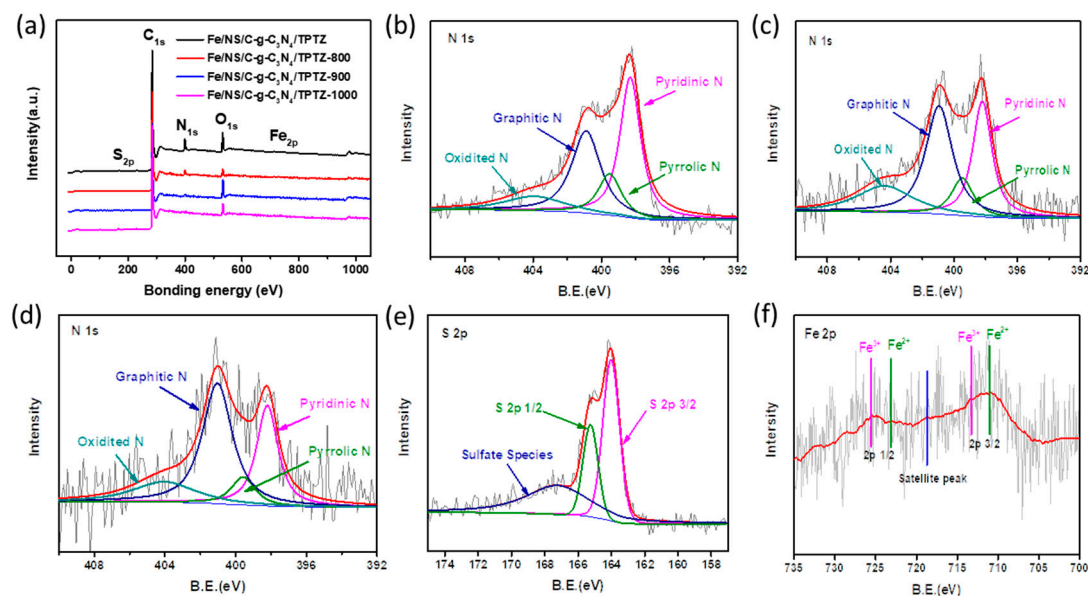


Figure 6. (a) XPS survey spectra of Fe/NS/C-g-C₃N₄/TPTZ and Fe/NS/C-g-C₃N₄/TPTZ-T (T = 800, 900, 1000); high-resolution N 1s spectra of (b) Fe/NS/C-g-C₃N₄/TPTZ-800, (c) Fe/NS/C-g-C₃N₄/TPTZ-900 and (d) Fe/NS/C-g-C₃N₄/TPTZ-1000; (e) high-resolution S 2p spectrum and (f) Fe 2p spectrum of Fe/NS/C-g-C₃N₄/TPTZ-1000.

The ORR activities of Fe/NS/C-g-C₃N₄/TPTZ-T (T = 800, 900, 1000) catalysts were measured in O₂-saturated 0.1 M KOH solution. For a comparison, commercial Pt/C (20 wt %) catalyst was also evaluated. As displayed in Figure 7a, after secondary heat treatment, the ORR activity of the Fe/NS/C-g-C₃N₄/TPTZ is further improved. Fe/NS/C-g-C₃N₄/TPTZ-800 and Fe/NS/C-g-C₃N₄/TPTZ-900 exhibit similar activity with the half-wave potential ($E_{1/2}$) of 0.863 V and 0.864 V (RHE), respectively. The best ORR activity is achieved at Fe/NS/C-g-C₃N₄/TPTZ-1000 with the onset and half-wave potential of 1.0 V and 0.868 V (RHE), respectively, higher than that of Pt/C catalyst (E_0 = 0.97 V, $E_{1/2}$ = 0.841 V). To evaluate the intrinsic catalytic activity, the mass activity (j_m) was calculated based on the Koutecky-Levich equation (Table S3). The Fe/NS/C-g-C₃N₄/TPTZ-1000 catalyst shows the best mass activity of 5.73 A g⁻¹ at 0.9 V, reaching up to 48.8% of that of Pt/C (11.73 A g⁻¹).

To explore the origin of the high ORR activity, we have probed the possible role of Fe and S within the Fe-NS/PC catalysts. As shown in Figure S2, Fe/N/C-g-C₃N₄/TPTZ-1000 without sulfur doping exhibits lower onset and half-wave potentials for the ORR than Fe/NS/C-g-C₃N₄/TPTZ-1000, indicating the promoting effects of sulfur co-doping. By sharp comparison, the NS/C-g-C₃N₄/TPTZ-1000 without Fe doping presents inferior activity, with the half-wave potential 64 mV lower than that of Fe/NS/C-g-C₃N₄/TPTZ-1000. These results definitely reflect the indispensable roles of Fe and S doping in Fe-NS/PC for high ORR activity. It is well known that SCN⁻ can strongly coordinate with Fe atoms. As shown in Figure S3, the Fe/NS/C-g-C₃N₄/TPTZ-1000 catalyst shows obvious ORR activity degradation after injecting 5 mM SCN⁻, the remaining ORR activity probably results from the N, S co-doped carbon materials. Interestingly, the ORR activity of the Fe/NS/C-g-C₃N₄/TPTZ-1000 can almost recover after rinsing and replacing with fresh electrolyte, indicating that Fe atoms are at least part of the ORR active sites.

Figure 7b shows the hydrogen peroxide yield (H₂O₂ %) and the electron transfer number (n) of Fe/NS/C-g-C₃N₄/TPTZ-1000 calculated from disk current (I_d) and ring current (I_r) obtained by rotating ring-disk electrode (RRDE) test. The H₂O₂ yield is lower than 1.0% over the whole potential range. The corresponding electron transfer number is calculated to be larger than 3.975. Notably, the H₂O₂ starts to generate at the potential lower than 0.8 V, where the ORR polarization curve has

reached the diffusion-limited current. These results indicate a direct four-electron pathway of ORR on the Fe/NS/C-g-C₃N₄/TPTZ-1000. The Tafel plots of Fe/NS/C-g-C₃N₄/TPTZ-1000 depicted in Figure 7c show the Tafel slope of 68 mV dec⁻¹, closed to that of Pt/C catalyst (73 mV dec⁻¹).

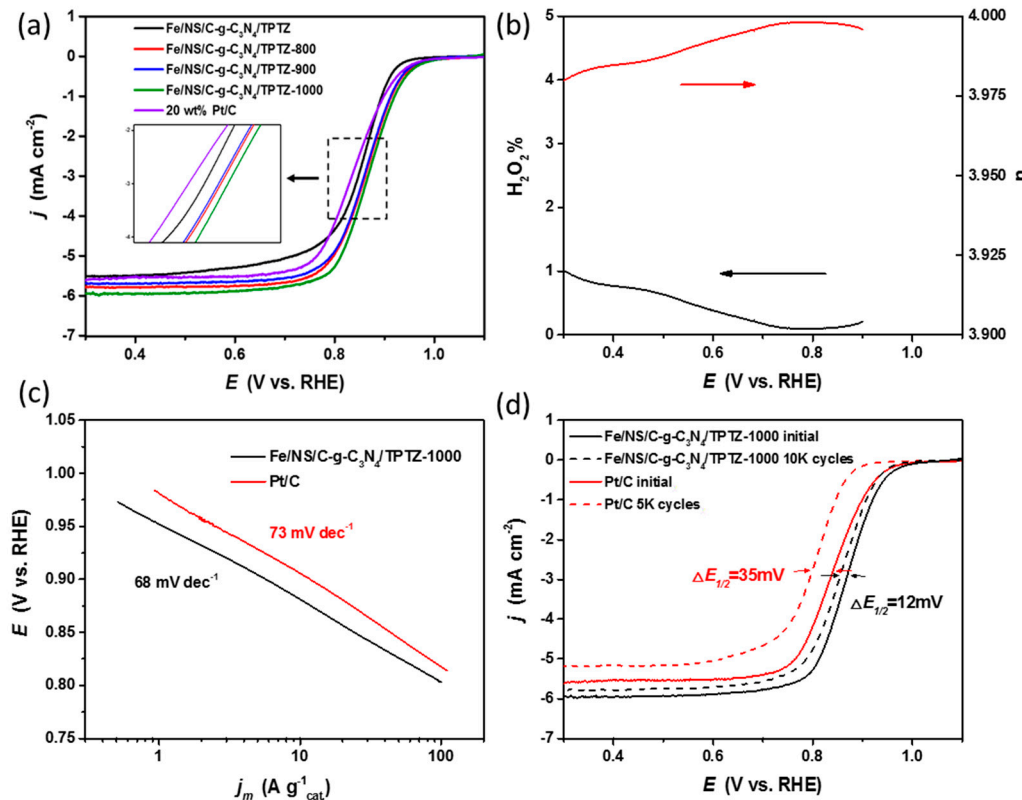


Figure 7. (a) ORR polarization curves of Fe/NS/C-g-C₃N₄/TPTZ, Fe/NS/C-g-C₃N₄/TPTZ-T ($T = 800, 900, 1000$) and Pt/C catalyst in O₂-saturated 0.1 M KOH solution with a rotational speed of 1600 rpm and at a scan rate of 10 mV/s; (b) hydrogen peroxide yield and electron transfer number of Fe/NS/C-g-C₃N₄/TPTZ-1000 catalyst, (c) Tafel plots of Fe/NS/C-g-C₃N₄/TPTZ-1000 and Pt/C; and (d) ORR polarization curves of Fe/NS/C-g-C₃N₄/TPTZ-1000 (before and after 10,000 potential cycles) and Pt/C (before and after 5000 potential cycles).

An accelerated durability test (ADT) was carried out to assess the durability of Fe/NS/C-g-C₃N₄/TPTZ-1000 catalyst by potential-cycling between 0.6 and 1.1 V at a scan rate of 50 mV s⁻¹ in O₂-saturated 0.1 M KOH. As shown in Figure 7d, after 10,000 cycles, the $E_{1/2}$ of Fe/NS/C-g-C₃N₄/TPTZ-1000 slightly decreases by 12 mV, demonstrating the superior durability of the Fe/NS/C-g-C₃N₄/TPTZ-1000 catalyst, due to the robust structure of Fe and N anchored in carbon matrix and the low yield of corrosive H₂O₂. In sharp contrast, the $E_{1/2}$ of Pt/C remarkably decreases by 35 mV after only 5000 cycles. The insufficient durability of the Pt/C might suffer from the aggregation of Pt nanoparticles.

To further evaluate the potential for practical application, the Fe/NS/C-g-C₃N₄/TPTZ-1000 was assembled into a homemade primary Zn-air battery as cathode catalyst. Figure 8a presents the polarization curves of Zn-air batteries with Fe/NS/C-g-C₃N₄/TPTZ-1000 and Pt/C as cathodes, respectively. The Zn-air battery with Fe/NS/C-g-C₃N₄/TPTZ-1000 catalyst exhibits an open-circuit voltage (OCV) of 1.385 V and a maximal power density of 225 mW cm⁻² at a temperature of ca. 25 °C, which is quite comparable to that of Pt/C with the OCV of 1.411 V and the maximal power density of 246 mW cm⁻². This performance outperforms the most of Zn-Air batteries utilizing analogous Fe-N-C cathode reported so far [37–40]. In the meantime, the long-term stability of a Zn-air battery

with Fe/NS/C-g-C₃N₄/TPTZ-1000 was also tested by recording the galvanostatic discharge curves. As presented in Figure 8b, the Zn-Air battery with Fe/NS/C-g-C₃N₄/TPTZ-1000 catalyst only presents a voltage loss of 4.03% after 20,000 s at a current density of 20 mA cm⁻². For the Pt/C, the output voltage loss reaches 8.17% under the same conditions, demonstrating the improved durability of the Fe/NS/C-g-C₃N₄/TPTZ-1000. The slight fluctuation may due to the disturbance of testing circumstance such as humidity, which cannot be completely avoided. These results suggest that the as-prepared Fe/NS/C-g-C₃N₄/TPTZ-1000 catalyst has great potential to replace the precious metal catalysts in practical application of Zn-air battery.

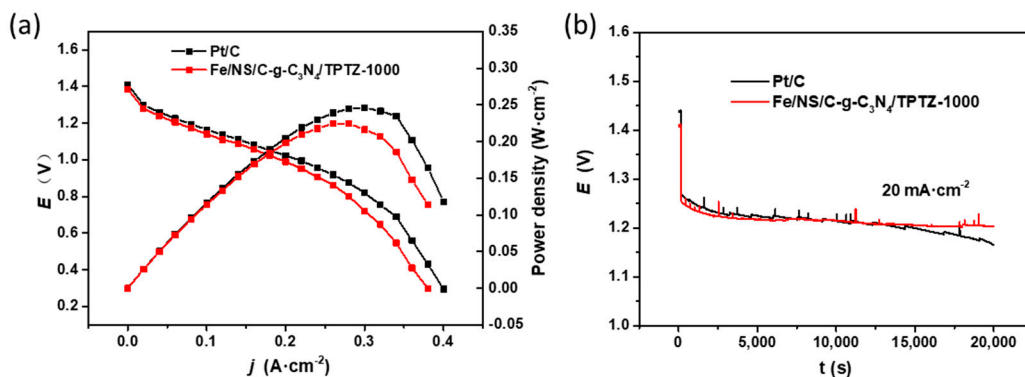


Figure 8. (a) Polarization curves and (b) discharge curves of Zn-air batteries with Fe/NS/C-g-C₃N₄/TPTZ-1000, and 20 wt % Pt/C as cathode catalysts at 298 K.

3. Experimental Section

3.1. Preparation of g-C₃N₄ Nanosheets

Bulk g-C₃N₄ powder was synthesized according to a procedure described in a previous paper [41]. Typically, dicyandiamide (Aldrich, Milwaukee, WI, USA, 99%) powder was placed in an alumina crucible with cover and heated at 550 °C for 4 h in air with a ramp rate of 2.3 °C/min. The obtained yellow agglomerates were grinded into powders. The light yellow g-C₃N₄ nanosheets were prepared by thermal etching of bulk g-C₃N₄ in air at 500 °C for 2 h with a ramp rate of 5 °C/min.

3.2. Catalyst Synthesis

Commercial Ketjenblack EC 600J (KJ 600) carbon black was first pretreated in 6.0 M HCl solution for 12 h to remove metal impurities and collected by filtration. The obtained carbon black was then treated in concentrated HNO₃ solution at 80 °C for 8 h to introduce carboxyl groups [42].

In a typical synthesis, 125 mg of 2,4,6-tri(2-pyridyl)-1,3,5-triazine (TPTZ, Adamas, Shanghai, China, 97%), 125 mg of g-C₃N₄ nanosheets, and 50 mg of acid-treated KJ600 were dispersed in 50 mL of alcohol under vigorous stirring for 30 min, then Fe(SCN)₃ solution, prepared by mixing FeCl₃ (0.2 M, 1.2 mL) and potassium thiocyanate (KSCN, 0.2 M, 3.6 mL) in 50 mL of alcohol, was added into the suspension and stirred for another 30 min. The solvent was then removed by rotary evaporation and vacuum drying at 80 °C for 3 h. The resulting powder was pyrolyzed at 800 °C in a N₂ atmosphere for 1 h with a ramp rate of 10 °C/min. The pyrolyzed sample was subjected to acid leaching in 0.5 M H₂SO₄ solution at 80 °C for 8 h to remove unstable and inactive species followed by filtration and thoroughly washed with ultrapure water. The sample was finally vacuum dried to obtain the Fe/NS/C-g-C₃N₄/TPTZ catalyst. As a comparison, Fe/NS/C-g-C₃N₄ and Fe/NS/C-TPTZ catalysts were prepared by the same procedure except using 250 mg of g-C₃N₄ or 250 mg of TPTZ as the single nitrogen precursor, respectively.

Moreover, the Fe/NS/C-g-C₃N₄/TPTZ sample was heat-treated again at 800 °C, 900 °C, and 1000 °C in a N₂ atmosphere for 3 h to obtain the Fe/NS/C-g-C₃N₄/TPTZ-T (T = 800, 900, 1000)

catalysts. The synthesis approaches for Fe/N/C-g-C₃N₄/TPTZ-1000 and NS/C-g-C₃N₄/TPTZ-1000 are the same as that for Fe/NS/C-g-C₃N₄/TPTZ-1000 without adding KSCN and FeCl₃, respectively.

3.3. Characterizations

The morphology and elemental mapping of the samples were analyzed using field-emission transmission electron microscopy (FE-TEM, JEM-2100F, JEOL Ltd., Tokyo, Japan) with a working voltage of 200 kV. XRD analysis was performed using a D8 advance powder X-ray diffractometer (Bruker, Karlsruhe, Germany) with a Cu Ka ($\lambda = 1.5418 \text{ \AA}$) at 0.2° s^{-1} . The elemental composition and chemical states were measured by XPS (K-Alpha, Thermo Scientific, Waltham, MA, USA) with an Al Ka X-ray source. The surface areas and pore structures were characterized using a Micromeritics ASAP 2020 instrument (Micromeritics Instrument Corp., Norcross, GA, USA).

3.4. Electrochemical Measurement

All electrochemical measurements were conducted on a bipotentiostat (CHI-730E, Shanghai Chenhua, Shanghai, China) equipped with a rotating disk electrode (RDE) or rotating ring-disk electrode (RRDE) system (PINE Inc., Durham, NC, USA) at room temperature. An Ag/AgCl electrode and a graphite plate were used as the reference and counter electrode, respectively. The potential has been experimentally corrected to the range of RHE by the following equation: $E(\text{RHE}) = E(\text{Ag/AgCl}) + 0.956 \text{ V}$. The electrolyte was O₂-saturated 0.1 M KOH solution.

For all Fe-NS/PC catalysts, 12 mg of catalyst was dispersed in the mixture of 0.5 mL of de-ionized water, 0.45 mL of isopropanol and 0.05 mL of 5 wt % Nafion solution (Aldrich) by sonication for 1 h to produce the ink. A certain volume of the catalyst ink was pipetted onto the pre-polished glassy carbon disk (0.196 cm² for RDE and 0.2475 cm² for RRDE) resulting a loading of 0.4 mg cm⁻². For commercial Pt/C catalyst (20 wt %, ElectroChem, Inc., Woburn, MA, USA), the ink was prepared by dispersing 10 mg catalyst in 1.0 mL of de-ionized water, 0.95 mL of isopropanol, and 0.05 mL of 5 wt % Nafion solution. The loading of the Pt/C catalyst was 0.1 mg cm⁻².

In RDE tests, ORR polarization curves were measured at a scan rate of 10 mV s⁻¹. The electrode rotational speed was 1600 rpm. The background current was determined by recording the voltammogram in N₂-saturated electrolyte. The accelerated durability tests (ADT) were carried out by cycling the potential in the range from 0.6 to 1.1 V in O₂-saturated electrolyte with a scan rate of 50 mV s⁻¹.

Hydrogen peroxide yield and the electron transfer number (n) can be calculated by the following equations with the potential of ring electrode fixed at 1.4 V (RHE) in RRDE:

$$\text{H}_2\text{O}_2 \% = 200\% \times \frac{\frac{I_r}{N}}{|I_d| + \frac{I_r}{N}} \quad (1)$$

$$n = 4 \times \frac{|I_d|}{|I_d| + \frac{I_r}{N}} \quad (2)$$

where I_d is the disk current, I_r is the ring current, $N = 0.37$ is the collection efficiency of the Pt ring.

3.5. Primary Zn-Air Battery Test

The cathode of the Zn-air battery was prepared by loading the Fe/NS/C-g-C₃N₄/TPTZ-1000 or 20 wt % Pt/C catalyst onto carbon fiber paper (3.0 × 4.0 cm) with a catalyst loading of 1.0 mg cm⁻². Electrolytic zinc powder was used as the anode. The electrolyte was 6.0 M KOH solution. Polarization curves and galvanostatic discharge curves were measured on Arbin battery testing system.

4. Conclusions

In summary, a Fe, N, S co-doped porous carbon as ORR electrocatalyst was developed based on the interaction of binary nitrogen precursors during the pyrolysis process. After secondary heat

treatment, the Fe/NS/C-g-C₃N₄/TPTZ-1000 catalyst displays superior ORR activity and durability in alkaline media, in comparison with the commercial Pt/C. Enhanced ORR activity and durability can be attributed to its good porous structure, high surface area, high contents of pyridinic N and graphitic N, and the synergy of N and S co-doping. Moreover, the Zn-air battery assembled with Fe/NS/C-g-C₃N₄/TPTZ-1000 as a cathode exhibits comparable power density and better stability than that of the Pt/C, demonstrating its potential for substituting precious metal catalysts in practical energy devices.

Supplementary Materials: The following are available online at <http://www.mdpi.com/2073-4344/8/4/158/s1>, Figure S1: Thermogravimetric analysis (TGA) of (a) g-C₃N₄ and (b) TPTZ under N₂ atmosphere, Figure S2: ORR polarization curves of Fe/N/C-g-C₃N₄/TPTZ-1000, NS/C-g-C₃N₄/TPTZ-1000 and Fe/NS/C-g-C₃N₄/TPTZ-1000 in O₂-saturated 0.1 M KOH solution with a rotational speed of 1600 rpm and a scan rate of 10 mV/s, Figure S3: The polarization curves of Fe/NS/C-g-C₃N₄/TPTZ-1000 catalyst before and after adding SCN[−] and after rinsing and replacing fresh O₂-saturated 0.1 M KOH solution, Table S1: The element contents of Fe/NS/C-g-C₃N₄, Fe/NS/C-TPTZ and Fe/NS/C-g-C₃N₄/TPTZ obtained by XPS, Table S2: The element contents of Fe/NS/C-g-C₃N₄/TPTZ-T (T = 800, 900, 1000) obtained by XPS, Table S3: Comparison of ORR activity of Fe/NS/C-g-C₃N₄/TPTZ, Fe/NS/C-g-C₃N₄/TPTZ-T (T = 800, 900, 1000) and Pt/C catalysts.

Acknowledgments: The financial supports from the National Key Research and Development Program of China (grant no. 2017YFA0206500) and the National Natural Science Foundation of China (grant no. 21673275, 21533005) are greatly appreciated.

Author Contributions: Xiao Liu, Chi Chen, Zhiqing Zou, and Hui Yang conceived and designed the experiments; Xiao Liu performed the experiments; Xiao Liu, Chi Chen, Qingqing Cheng, and Liangliang Zou analyzed the data; Xiao Liu and Chi Chen wrote the paper; Zhiqing Zou and Hui Yang managed all the experiments and the writing process as the corresponding authors.

Conflicts of Interest: The authors declare no conflict of interest.

References

- Cui, X.; Yang, S.; Yan, X.; Leng, J.; Shuang, S.; Ajayan, P.M.; Zhang, Z. Pyridinic-Nitrogen-Dominated Graphene Aerogels with Fe-N-C Coordination for Highly Efficient Oxygen Reduction Reaction. *Adv. Funct. Mater.* **2016**, *26*, 5708–5717. [[CrossRef](#)]
- Zhu, Z.; Yang, Y.; Guan, Y.; Xue, J.; Cui, L. Constructing of cobalt-embedded in nitrogen-doped carbon material with desired porosity derived from MOFs confined growth within graphene aerogel as a superior catalyst towards HER and ORR. *J. Mater. Chem. A* **2016**, *4*, 15536–15545. [[CrossRef](#)]
- Yang, J.; Liu, D.J.; Kariuki, N.N.; Chen, L.X. Aligned carbon nanotubes with built-in FeN₄ active sites for electrocatalytic reduction of oxygen. *Chem. Commun.* **2008**, *36*, 329–331. [[CrossRef](#)]
- Zeng, L.; Cui, X.; Chen, L.; Ye, T.; Huang, W.; Ma, R.; Zhang, X.; Shi, J. Non-noble bimetallic alloy encased in nitrogen-doped nanotubes as a highly active and durable electrocatalyst for oxygen reduction reaction. *Carbon* **2017**, *114*, 347–355. [[CrossRef](#)]
- Liu, H.; Shi, Z.; Zhang, J.; Zhang, L.; Zhang, J. Ultrasonic spray pyrolyzed iron-polypyrrole mesoporous spheres for fuel cell oxygen reduction electrocatalysts. *J. Mater. Chem.* **2009**, *19*, 468–470. [[CrossRef](#)]
- Liang, H.W.; Wei, W.; Wu, Z.S.; Feng, X.; Müllen, K. Mesoporous Metal-Nitrogen-Doped Carbon Electrocatalysts for Highly Efficient Oxygen Reduction Reaction. *J. Am. Chem. Soc.* **2013**, *135*, 16002–16005. [[CrossRef](#)] [[PubMed](#)]
- Wu, G.; Zelenay, P. Nanostructured nonprecious metal catalysts for oxygen reduction reaction. *Acc. Chem. Res.* **2013**, *46*, 1878–1889. [[CrossRef](#)] [[PubMed](#)]
- Zhang, J.; Dai, L. Heteroatom-doped graphitic carbon catalysts for efficient electrocatalysts of oxygen reduction reaction. *ACS Catal.* **2015**, *5*, 7244–7253. [[CrossRef](#)]
- Jia, Q.; Ramaswamy, N.; Hafiz, H.; Tylus, U.; Strickland, K.; Wu, G.; Barbiellini, B.; Bansil, A.; Holby, E.F.; Zelenay, P. Experimental observation of redox-induced Fe–N switching behavior as a determinant role for oxygen reduction activity. *ACS Nano* **2015**, *9*, 12496–12505. [[CrossRef](#)] [[PubMed](#)]
- Kone, I.; Xie, A.; Tang, Y.; Chen, Y.; Liu, J.; Chen, Y.; Sun, Y.; Yang, X.; Wan, P. Hierarchical Porous Carbon Doped with Iron-Nitrogen-Sulfur for Efficient Oxygen Reduction Reaction. *ACS Appl. Mater. Interfaces* **2017**, *9*, 20963–20973. [[CrossRef](#)] [[PubMed](#)]

11. Yu, H.; Fisher, A.; Cheng, D.; Cao, D. Cu, N-codoped Hierarchical Porous Carbons as Electrocatalysts for Oxygen Reduction Reaction. *ACS Appl. Mater. Interfaces* **2016**, *8*, 21431–21439. [[CrossRef](#)] [[PubMed](#)]
12. Qiao, M.; Tang, C.; He, G.; Qiu, K.; Binions, R.; Parkin, I.; Zhang, Q.; Guo, Z.; Titirici, M. Graphene/nitrogen-doped porous carbon sandwiches for the metal-free oxygen reduction reaction: Conductivity versus active sites. *J. Mater. Chem. A* **2016**, *4*, 12658–12666. [[CrossRef](#)]
13. Lefèvre, M.; Proietti, E.; Jaouen, F.; Dodelet, J.P. Iron-based catalysts with improved oxygen reduction activity in polymer electrolyte fuel cells. *Science* **2009**, *324*, 71–74. [[CrossRef](#)] [[PubMed](#)]
14. Li, Z.; Sun, H.; Wei, L.; Jiang, W.J.; Wu, M.; Hu, J.S. Lamellar Metal Organic Framework-Derived Fe–N–C Non-Noble Electrocatalysts with Bimodal Porosity for Efficient Oxygen Reduction. *ACS Appl. Mater. Interfaces* **2017**, *9*, 5272–5278. [[CrossRef](#)] [[PubMed](#)]
15. Gupta, S.; Zhao, S.; Ogoke, O.; Lin, Y.; Xu, H.; Wu, G. Engineering Favorable Morphology and Structure of Fe-N-C Oxygen-Reduction Catalysts through Tuning of Nitrogen/Carbon Precursors. *ChemSusChem* **2017**, *10*, 774–785. [[CrossRef](#)] [[PubMed](#)]
16. Fu, X.; Zamani, P.; Choi, J.Y.; Hassan, F.M.; Jiang, G.; Higgins, D.C.; Zhang, Y.; Hoque, M.A.; Chen, Z. In Situ Polymer Graphenization Ingrained with Nanoporosity in a Nitrogenous Electrocatalyst Boosting the Performance of Polymer-Electrolyte-Membrane Fuel Cells. *Adv. Mater.* **2016**, *29*, 1604456. [[CrossRef](#)] [[PubMed](#)]
17. Chung, H.T.; Cullen, D.A.; Higgins, D.; Snead, B.T.; Holby, E.F.; More, K.L.; Zelenay, P. Direct atomic-level insight into the active sites of a high-performance PGM-free ORR catalyst. *Science* **2017**, *357*, 479–484. [[CrossRef](#)] [[PubMed](#)]
18. Wang, Y.C.; Lai, Y.J.; Song, L.; Zhou, Z.Y.; Liu, J.G.; Wang, Q.; Yang, X.D.; Chen, C.; Shi, W.; Zheng, Y.P.; et al. S-Doping of an Fe/N/C ORR Catalyst for Polymer Electrolyte Membrane Fuel Cells with High Power Density. *Angew. Chem. Int. Ed.* **2015**, *127*, 10045–10048. [[CrossRef](#)]
19. Chen, P.; Zhou, T.; Xing, L.; Xu, K.; Tong, Y.; Xie, H.; Zhang, L.; Yan, W.; Chu, W.; Wu, C. Atomically Dispersed Iron-Nitrogen Species as Electrocatalysts for Bifunctional Oxygen Evolution and Reduction Reactions. *Angew. Chem. Int. Ed.* **2017**, *56*, 610–614. [[CrossRef](#)] [[PubMed](#)]
20. Tian, J.; Morozan, A.; Sougrati, M.T.; Chenitz, R.; Dodelet, J.P.; Jones, D.; Jaouen, F. Optimized synthesis of Fe/N/C cathode catalysts for PEM fuel cells: A matter of iron-ligand coordination strength. *Angew. Chem. Int. Ed.* **2013**, *52*, 6867–6870. [[CrossRef](#)] [[PubMed](#)]
21. Yang, L.; Kong, J.; Zhou, D.; Ang, J.M.; Phua, S.L.; Yee, W.A.; Liu, H.; Huang, Y.; Lu, X. Transition-Metal-Ion-Mediated Polymerization of Dopamine: Mussel-Inspired Approach for the Facile Synthesis of Robust Transition-Metal Nanoparticle–Graphene Hybrids. *Chem. Eur. J.* **2014**, *20*, 7776–7783. [[CrossRef](#)] [[PubMed](#)]
22. Zhou, D.; Yang, L.; Yu, L.; Kong, J.; Yao, X.; Liu, W.; Xu, Z.; Lu, X. Fe/N/C hollow nanospheres by Fe(III)-dopamine complexation-assisted one-pot doping as nonprecious-metal electrocatalysts for oxygen reduction. *Nanoscale* **2015**, *7*, 1501–1509. [[CrossRef](#)] [[PubMed](#)]
23. Jaouen, F.; Herranz, J.; Lefèvre, M.; Dodelet, J.P.; Kramm, U.I.; Herrmann, I.; Bogdanoff, P.; Maruyama, J.; Nagaoka, T.; Garsuch, A. Cross-laboratory experimental study of non-noble-metal electrocatalysts for the oxygen reduction reaction. *ACS Appl. Mater. Interfaces* **2009**, *1*, 1623–1639. [[CrossRef](#)] [[PubMed](#)]
24. Jaouen, F.; Lefèvre, M.; Dodelet, J.P.; Cai, M. Heat-Treated Fe/N/C Catalysts for O₂ Electroreduction: Are Active Sites Hosted in Micropores? *J. Phys. Chem. B* **2006**, *110*, 5553–5558. [[CrossRef](#)] [[PubMed](#)]
25. Yasuda, S.; Furuya, A.; Uchibori, Y.; Kim, J.; Murakoshi, K. Iron–Nitrogen-Doped Vertically Aligned Carbon Nanotube Electrocatalyst for the Oxygen Reduction Reaction. *Adv. Funct. Mater.* **2016**, *26*, 738–744. [[CrossRef](#)]
26. Choi, I.A.; Kwak, D.H.; Han, S.B.; Park, J.Y.; Park, H.S.; Ma, K.B.; Kim, D.H.; Won, J.E.; Park, K.W. Doped porous carbon nanostructures as non-precious metal catalysts prepared by amino acid glycine for oxygen reduction reaction. *Appl. Catal. B Environ.* **2017**, *211*, 235–244. [[CrossRef](#)]
27. Liang, W.; Chen, J.; Liu, Y.; Chen, S. Density-functional-theory calculation analysis of active sites for four-electron reduction of O₂ on Fe/N-doped graphene. *ACS Catal.* **2014**, *4*, 4170–4177. [[CrossRef](#)]
28. Xiao, H.; Shao, Z.G.; Zhang, G.; Gao, Y.; Lu, W.; Yi, B. Fe–N–carbon black for the oxygen reduction reaction in sulfuric acid. *Carbon* **2013**, *57*, 443–451. [[CrossRef](#)]
29. Saidi, W.A. Oxygen reduction electrocatalysis using N-doped graphene quantum-dots. *J. Phys. Chem. Lett.* **2013**, *4*, 4160–4165. [[CrossRef](#)]

30. Liang, J.; Jiao, Y.; Jaroniec, M.; Qiao, S.Z. Sulfur and nitrogen dual-doped mesoporous graphene electrocatalyst for oxygen reduction with synergistically enhanced performance. *Angew. Chem. Int. Ed.* **2012**, *51*, 11496–11500. [CrossRef] [PubMed]
31. Jiang, T.; Wang, Y.; Wang, K.; Liang, Y.; Wu, D.; Tsiaikaras, P.; Song, S. A novel sulfur-nitrogen dual doped ordered mesoporous carbon electrocatalyst for efficient oxygen reduction reaction. *Appl. Catal. B Environ.* **2016**, *189*, 1–11. [CrossRef]
32. Ai, W.; Luo, Z.; Jiang, J.; Zhu, J.; Du, Z.; Fan, Z.; Xie, L.; Zhang, H.; Huang, W.; Yu, T. Nitrogen and sulfur codoped graphene: Multifunctional electrode materials for high-performance Li-ion batteries and oxygen reduction reaction. *Adv. Mater.* **2014**, *26*, 6186–6192. [CrossRef] [PubMed]
33. Chen, C.; Yang, X.D.; Zhou, Z.Y.; Lai, Y.J.; Rauf, M.; Wang, Y.; Pan, J.; Zhuang, L.; Wang, Q.; Wang, Y.C. Aminothiazole-derived N, S, Fe-doped graphene nanosheets as high performance electrocatalysts for oxygen reduction. *Chem. Commun.* **2015**, *51*, 17092–17095. [CrossRef] [PubMed]
34. Shen, H.; Gracia-Espino, E.; Ma, J.; Zang, K.; Luo, J.; Wang, L.; Gao, S.; Mamat, X.; Hu, G.; Wagberg, T. Synergistic Effects between Atomically Dispersed Fe–N–C and C–S–C for the Oxygen Reduction Reaction in Acidic Media. *Angew. Chem. Int. Ed.* **2017**, *56*, 13800–13804. [CrossRef] [PubMed]
35. Zeng, S.; Lyu, F.; Nie, H.; Zhan, Y.; Bian, H.; Tian, Y.; Li, Z.; Wang, A.; Lu, J.; Li, Y.Y. Facile fabrication of N/S-doped carbon nanotubes with Fe_3O_4 nanocrystals enchased for lasting synergy as efficient oxygen reduction catalysts. *J. Mater. Chem. A* **2017**, *5*, 13189–13195. [CrossRef]
36. Ren, G.; Lu, X.; Li, Y.; Zhu, Y.; Dai, L.; Jiang, L. Porous Core–Shell Fe_3C Embedded N-doped Carbon Nanofibers as an Effective Electrocatalysts for Oxygen Reduction Reaction. *ACS Appl. Mater. Interfaces* **2016**, *8*, 4118–4125. [CrossRef] [PubMed]
37. Cao, L.; Li, Z.; Gu, Y.; Li, D.; Su, K.; Yang, D.; Cheng, B. Rational design of N-doped carbon nanobox-supported $\text{Fe}/\text{Fe}_2\text{N}/\text{Fe}_3\text{C}$ nanoparticles as efficient oxygen reduction catalysts for Zn-air batteries. *J. Mater. Chem. A* **2017**, *5*, 11340–11347. [CrossRef]
38. Zhao, Y.; Lai, Q.; Wang, Y.; Zhu, J.; Liang, Y.Y. Interconnected Hierarchically Porous Fe, N-Codoped Carbon Nanofibers as Efficient Oxygen Reduction Catalysts for Zn-Air Batteries. *ACS Appl. Mater. Interfaces* **2017**, *9*, 16178–16186. [CrossRef] [PubMed]
39. Yang, J.; Toshimitsu, F.; Yang, Z.; Fujigaya, T.; Nakashima, N. Pristine carbon nanotube/iron phthalocyanine hybrids with a well-defined nanostructure show excellent efficiency and durability for oxygen reduction reaction. *J. Mater. Chem. A* **2016**, *5*, 1184–1191. [CrossRef]
40. Cai, P.; Hong, Y.; Ci, S.; Wen, Z. In situ integration of CoFe alloy nanoparticles with nitrogen-doped carbon nanotubes as advanced bifunctional cathode catalysts for Zn-air batteries. *Nanoscale* **2016**, *8*, 20048–20055. [CrossRef] [PubMed]
41. Niu, P.; Zhang, L.; Liu, G.; Cheng, H.M. Graphene-like carbon nitride nanosheets for improved photocatalytic activities. *Adv. Funct. Mater.* **2012**, *22*, 4763–4770. [CrossRef]
42. Choi, J.Y.; Hsu, R.S.; Chen, Z. Highly active porous carbon-supported nonprecious metal-N electrocatalyst for oxygen reduction reaction in PEM fuel cells. *J. Phys. Chem. C* **2010**, *114*, 8048–8053. [CrossRef]



© 2018 by the authors. Licensee MDPI, Basel, Switzerland. This article is an open access article distributed under the terms and conditions of the Creative Commons Attribution (CC BY) license (<http://creativecommons.org/licenses/by/4.0/>).